Materials Science and Engineering B 266 (2021) 115044

Contents lists available at ScienceDirect

Materials Science & Engineering B

journal homepage: www.elsevier.com/locate/mseb

Exploring the composition, phase separation and structure of AgFe alloys for magneto-optical applications

Walker L. Boldman [a], David A. Garfinkel [a], Robyn Collette [a], Cameron S. Jorgenson [a], Dhiren K. Pradhan [a], Dustin A. Gilbert [a], Philip D. Rack [a,b,*]

[a] Department of Materials Science and Engineering, University of Tennessee, Knoxville, TN 37996, USA
[b] Center for Nanophase Materials Sciences, Oak Ridge National Laboratory, Oak Ridge, TN 37831, USA

ARTICLE INFO

Keywords:
Bimetallic alloys
Magneto-plasmonics
Thin films
Phase separated alloys
Cosputtered alloys

ABSTRACT

Bimetallic alloys with large discrepancies in atomic radii and crystal structure typically yield systems that are highly immiscible, even at high temperatures. The Ag_xFe_{1-x} binary system has limited solid and liquid solubility and thus phase separated Ag + Fe alloys should result. Furthermore, Ag has interesting plasmonic properties and Fe is a strong ferromagnet, thus magneto-plasmonic nanoparticles/films should result due to their phase separation. We have leveraged a combinatorial sputter deposition to synthesize thin films with a large Ag_xFe_{1-x} ($0.19 < x < 0.84$) phase space to correlate the composition and structure to the optical and magnetic properties for both as-deposited and annealed compositions.

1. Introduction:

Bimetallic systems have been studied for a wide variety of functional applications, including plasmonics [1–3] surface-enhanced Raman scattering [4] biomedicine [5–7] and others. Fe-based binary alloys are of particular interest for their structural and outstanding magnetic properties with large magnetization [8,9]. Further, the combination of a magnetic Fe compound, $Fe_{3-x}O_4$, with a plasmonic metal (Au), has been shown to produce magneto-plasmonic bi-functionality [6,7,10,11]. Magneto-optical materials with ferromagnetic/superparamagnetic and plasmonic properties have been explored for dual magnetic imaging and photothermal cancer therapies as well as magnetically enhanced photothermal therapy [5,7,11,12]. As an alternative to Au, Ag possesses a greater plasmonic quality factor, while also being immiscible with Fe. Fe and Ag have different crystal structures (BCC vs FCC), as well as a large discrepancy in atomic radii (140 pm vs 160 pm), causing the system to be immiscible, even in the liquid phase up to 4800 K. Sputter deposition, however, has successfully proven to be an effective method of obtaining metastable alloys which can extend the solubility limits [13]. Earlier work exploring this binary system by Takao et al. involved co-evaporation and magnetic measurement of a $Ag_{0.5}Fe_{0.5}$ system, showing changes in coercivity as a function of heat treatment [14]. Later work included Mössbauer spectroscopy of evaporated $Ag_{0.99}Fe_{0.01}$ and $Ag_{0.7}Fe_{0.3}$ alloys, detailing alloy formation of nanocrystalline grains [15,16] as well as work detailing a shift in magnetic moment and lattice size across the Ag-Fe phase diagram [13]. Notably, the vapor quenched films demonstrated composition regions with all FCC (Ag-rich), all BCC (Fe-Rich) and mixed phases with supersaturated compositions. The magnetic influence of Fe and its atomic volume in various binary systems, including $Ag_{0.5}Fe_{0.5}$, has also been calculated [17]. In this paper, we systematically investigate the optical properties, magnetic properties, and crystal structure of the Ag_xFe_{1-x} alloy system sputtered across a wide range of phase space ($0.19 < x < 0.84$) in the metastable as-deposited and phase-separated annealed form.

2. Materials and methods

2.1. Sputtering

In this study, 300 nm of Ag_xFe_{1-x} films were deposited via RF magnetron sputtering, where the Ag and Fe were co-sputtered from elemental targets in order to control the composition and to induce a compositional gradient. Sputtering was carried out at a base pressure of 1×10^{-7} Torr, a working pressure of 5 mTorr with an Ar gas flow rate of 25 sccm. The powers applied to the Ag and Fe targets were 30 W and 140 W, respectively, which yield similar sputtering rates of 2 nm/min. The substrate, a 25 × 100 mm [1 0 0] polished Si wafer strip, was oriented such that one end was positioned near the Ag sputter target, and

* Corresponding author at: Department of Materials Science and Engineering, University of Tennessee, Knoxville, TN 37996, USA.
E-mail address: prack@utk.edu (P.D. Rack).

https://doi.org/10.1016/j.mseb.2021.115044
Received 16 June 2020; Accepted 5 January 2021
Available online 18 January 2021

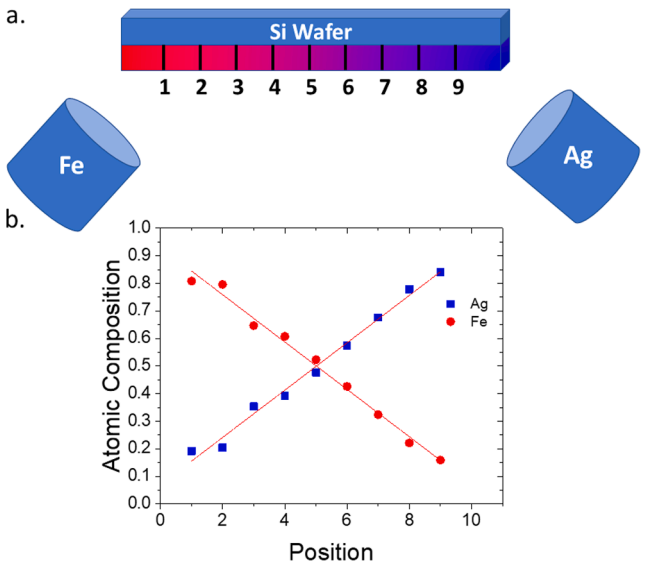

Fig. 1. a) Schematic illustrating the location of the sputtering targets and the sample positions. b) Measured EDS composition as a function of position and linear fit to the data relative to position. Sample size is 25 × 100 mm, with 10 mm between each position in both (a) and (b).

the other near the Fe sputter target (see diagram in Fig. 1), thus creating a composition gradient across the wafer, where one end is Ag-rich, and the other Fe-rich.

2.2. Energy dispersive X-ray spectroscopy

To determine the compositions of the samples, a series of Energy Dispersive X-ray Spectroscopy (EDS) scans were performed along the composition gradient in 10 mm increments using a Carl Zeiss EVO SEM. The atomic composition for the sample, Fig. 1, shows a relatively linear gradient of 0.86 at.%/mm across the wafer with an approximately equiatomic composition at the wafer center.

2.3. X-ray diffraction

X-ray diffraction (XRD) and phase identification was carried out using a Malvern Panalytical X'Pert3 MRD in a grazing incidence geometry, illuminating a 4 × 9 mm region. The substrate was oriented such that the long axis of the X-ray beam was perpendicular to the composition gradient, with the 4 mm beam width capturing a compositional range of ≈3.4 at.%. The incident angle was fixed at 12° and the detector angle was swept from 25° to 90°. Measurements were taken on both the as-deposited sample as well as a sample that was annealed at 873 K under vacuum for 1 h.

2.4. TEM

In-situ grain growth and phase separation experiments were performed by depositing a 20 nm thick film of $Ag_{0.5}Fe_{0.5}$ on a transmission electron microscope (TEM) membrane, then using a monochromated Carl Zeiss LIBRA 200 MC (S)TEM equipped with a laser delivery system (Waviks Inc.) to photothermally heat the sample [18]. The operating voltage was set to 200 kV and TEM bright field and high angle annular dark field (HAADF) scanning transmission electron micrographs (STEM) images were collected at 10 kX and 30 kX magnification. Selected area electron diffraction (SAED) patterns were also collected using a 5 μm aperture and radially averaged and normalized as described previously [19].

2.5. Electron energy loss spectroscopy (EELS)

STEM EELS was conducted on a Zeiss Libra TEM with an accelerating voltage of 200 keV, a convergence semi-angle of 0 mrad, and a collection semi-angle of 100 mrad. For data acquisition, a 0.5 μm monochromator slit with a dispersion of 30 meV per channel was used. The spectrum image was collected using a 29 × 23 grid of 4.4 nm square pixels and a dwell time of 0.02 s.

2.6. Ellipsometry

To measure the complex dielectric function, a J.A. Woolam M-2000U variable-angle spectroscopic ellipsometer was used, and data were collected in an energy range of 1.24–5.06 eV. No dispersion model was used to fit the results, as no suitable model for polycrystalline alloy films exists due to the complex phase structure, crystalline size, and energy band composition. Instead, Re(ε) and Im(ε) were obtained via point-by-point fitting of the calculated data.

2.7. Magnetometry

Magnetometry measurements were performed using a vibrating sample magnetometer (VSM) at temperatures between 1.9 K and 400 K. Temperature dependent magnetization (M-T) measurements in field cooled regime were performed by heating the sample to 400 K, applying a static 5 mT magnetic field, then cooling to 1.9 K while measuring the magnetization. The sample was then heated back to 400 K, a static magnetic field of 8.5 T was applied, and the sample was cooled to 1.9 K. Major hysteresis loops were recorded by measuring the magnetization versus magnetic field, M-H, at fixed temperatures. Measurements were performed on ten samples – five compositions, each as-deposited and annealed. The results were normalized to the volume of the measured films.

3. Results and discussion

In order to better correlate atomic composition and thickness to the

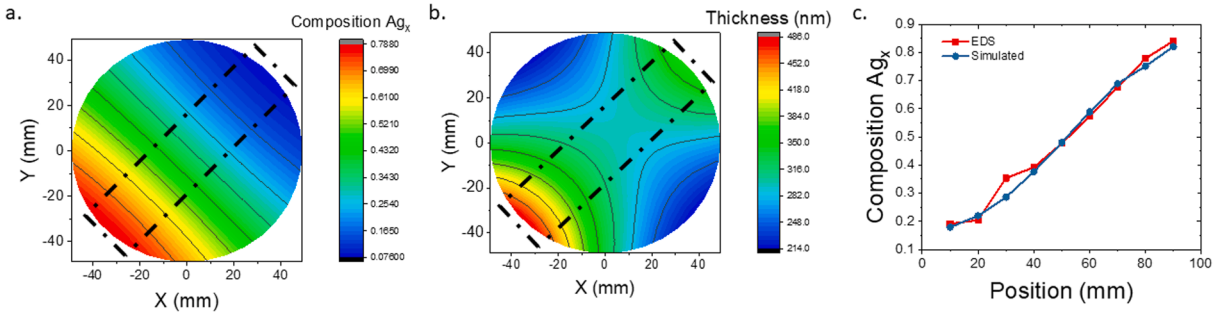

Fig. 2. 2D projection map of (a) Ag composition (x) in the Ag_xFe_{1-x}, (b) total thickness, and (c) plot comparing experimental Ag EDS composition and calculated Ag composition versus position on the substrate. Both maps are plotted for a 100 mm diameter wafer, with a dashed area indicating the 25 × 100 mm sample region.

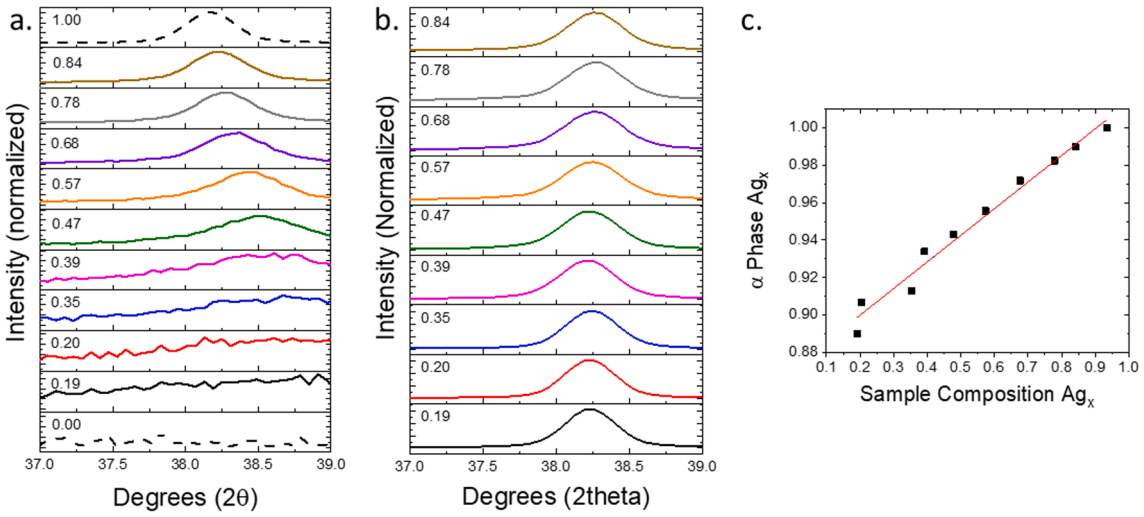

Fig. 3. Plot of the Ag (1 1 1) XRD peak, both as-deposited (a) and after annealing (b). For both (a) and (b), the peaks are labeled as a function of Ag sample composition as determined by EDS, as shown in Fig. 1. The atomic composition of the as-deposited Ag peak in (a) is plotted in (c) also as a function of Ag sample composition. In (a), the dashed lines indicate XRD taken from reference samples.

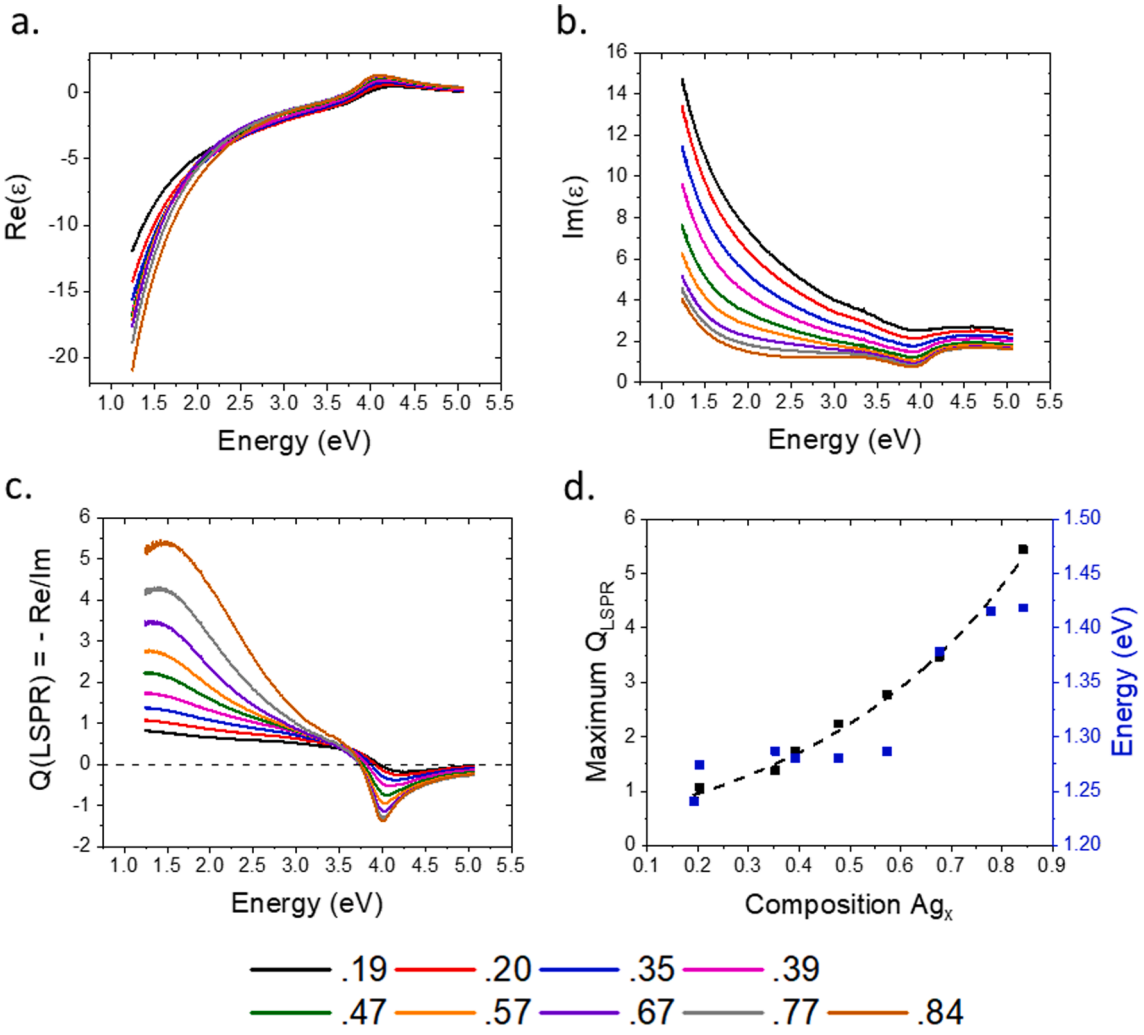

Fig. 4. Real (a) and imaginary (b) parts of the dielectric function for the annealed films, (c) corresponding Q_{LSPR} factors, and (d) maximum Q_{LSPR} and peak energy as a function of sample composition. Panels a–c are plotted for the different of Ag concentrations, as shown in the legend.

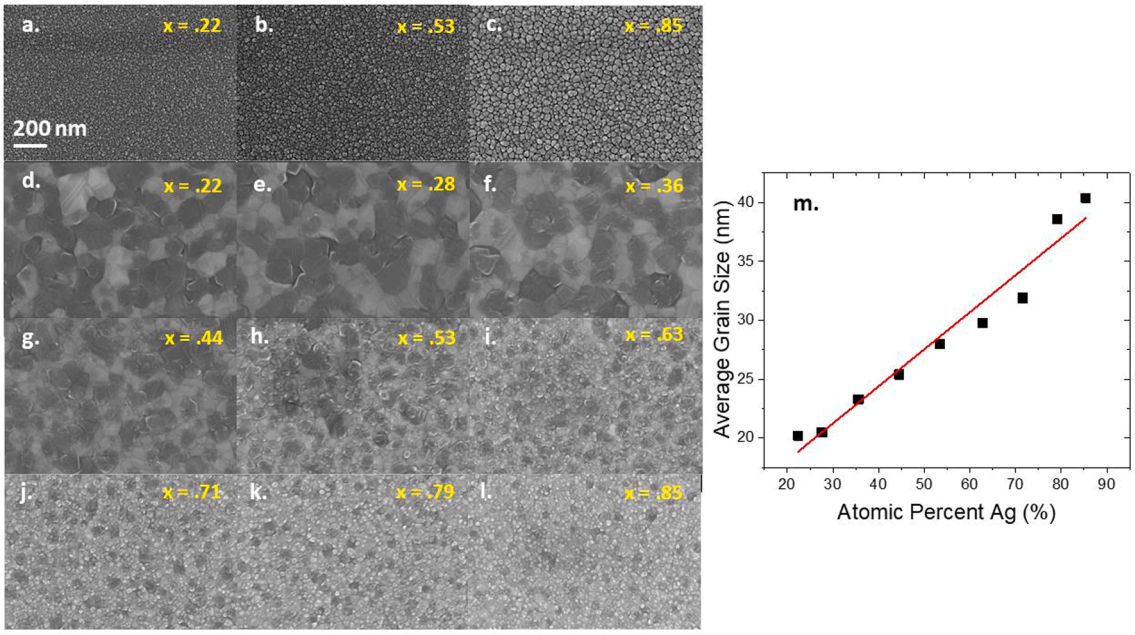

Fig. 5. SEM images of the as-deposited Ag_xFe_{1-x} film (a–c); SEM images of the Ag_xFe_{1-x} film annealed at 873 °C for 1 h under vacuum (d–l); (m) average grain size (diameter) in the as-deposited sample as a function of Ag composition. In a-l, the scale bar (bottom left of a) is 200 nm and applies to all the SEM images.

structural and optical properties of these alloys, a computational model was developed to estimate the film composition and thickness as a function of position across the 100 mm diameter substrate. This model is capable of predicting the atomic composition at any point on the substrate based on the sputtering rates of the individual sputtering sources, their material properties, as well as the necessary angular distribution of species emanating from the target.

For this model, each of the four sputter guns in this deposition system is modeled as an individual Knudson surface source, where the sputtering flux per unit area is given by the equation

$$\frac{d\overline{M_s}}{dA_s} = \frac{\overline{M_T}(n+1)cos^n\varphi cos\theta}{2\pi r^2} \quad (1)$$

where dM_s/dA_s is the mass deposited per unit area and M_T is the total sputtered mass from the target. Here, φ is the angle between the target surface normal and a line extending from the center of the target to a given point on the substrate surface, n is the degree of flux forward peaking, and has been determined experimentally to be ≈12 [20] due to the targets being positioned inside 50 mm tall stainless steel chimneys in order to minimize cross-contamination. As the targets are not perpendicular to the substrate, θ is introduced, and is defined as the angle between the substrate surface normal and a line extending from the center of the target surface to a given point on the substrate surface. Finally, *r* is the distance from the center of the target to a given point on the substrate surface.

The computational estimates of the substrate composition and thickness are shown in Fig. 2, with a dashed box indicating sample substrate and orientation relative to whole 100 mm diameter wafer. The results of Fig. 2a and the EDS results in Fig. 1 show good agreement.

As silver and iron are immiscible at room temperature, thermodynamically we expect the alloy to be phase-separated. Fig. 3 illustrates the FCC-derived (1 1 1) XRD peaks as a function of position for (a) the as-deposited and (b) annealed films. In the as-deposited samples, as the Fe concentration increases, the Ag (1 1 1) peak shifts to a higher 2θ values, indicating a decrease in lattice size. The atomic radius of silver is 160 pm and the lattice parameter of FCC silver is 0.409 nm, whereas the atomic radius of iron is 140 pm and the lattice parameter of BCC iron is 0.2856 nm. The persistence of the (1 1 1) peak across virtually all compositions and the decrease in the lattice parameter suggests that the smaller iron atoms substitutionally occupy the silver lattice positions, forming a metastable solid solution in the alpha (FCC) configuration. The amount of iron in this alpha phase can be calculated assuming Vegard's Law based on the atomic radii, as plotted in (c). Up to ≈12% of Fe is accommodated in the silver lattice, which is supersaturated relative to the room temperature thermodynamically limited (<1%) miscibility of Fe in Ag. After annealing, the (1 1 1) diffraction peak maintains a constant position over the composition range, indicating the out-diffusion of the supersaturated Fe and phase separation into nearly pure Fe and Ag phases. This is further explored in the TEM section.

The as-deposited films demonstrate a continuous shift in the dielectric constant as the film composition varies from iron rich to silver-rich, as shown in Fig. 4. Not surprisingly, as the silver concentration is increased, the localized surface plasmon resonance (LSPR) quality factor (Q), which measures the suitability of an alloy as a plasmonic material, increases significantly (Fig. 4c and d). Additionally, the peak in the Q factor over the spectroscopic range measured shifts to higher energy side with increasing silver concentration. In the silver-rich region, Re(ε) has a large negative value and a small Im(ε) value, demonstrating good low-energy plasmonic behavior.

To verify and characterize the phase separation, scanning electron microscopy (SEM) images were taken before and after annealing of the samples, where images were taken every 10 mm. Before annealing, the AgFe films are nanogranular across the sample gradient with very little phase contrast, as shown in Fig. 5. The grain size increases linearly as the composition shifts from iron-rich to silver-rich (Fig. 5m), which is explained by silver's higher melting temperature and larger crystal structure. After annealing for 1 h at 873 K in vacuum, the Ag and Fe phase separate, and grain growth is induced. On the iron-rich side (positions 1–4), the grain size stays roughly the same size as the as-deposited film (35–45 nm in diameter), but the Ag (lighter) and Fe (darker) separate and form distinct grains throughout the film. Once the film reaches an equiatomic composition, larger grain sizes are observed, forming Fe rich and Ag rich regions. Moving towards the Ag rich side (positions 6–9), the Fe grains become smaller as the phase fraction decreases, forming islands in the semi-continuous Ag film. Excess silver also starts to precipitate out of the film, creating particles as large as 2 μm in diameter.

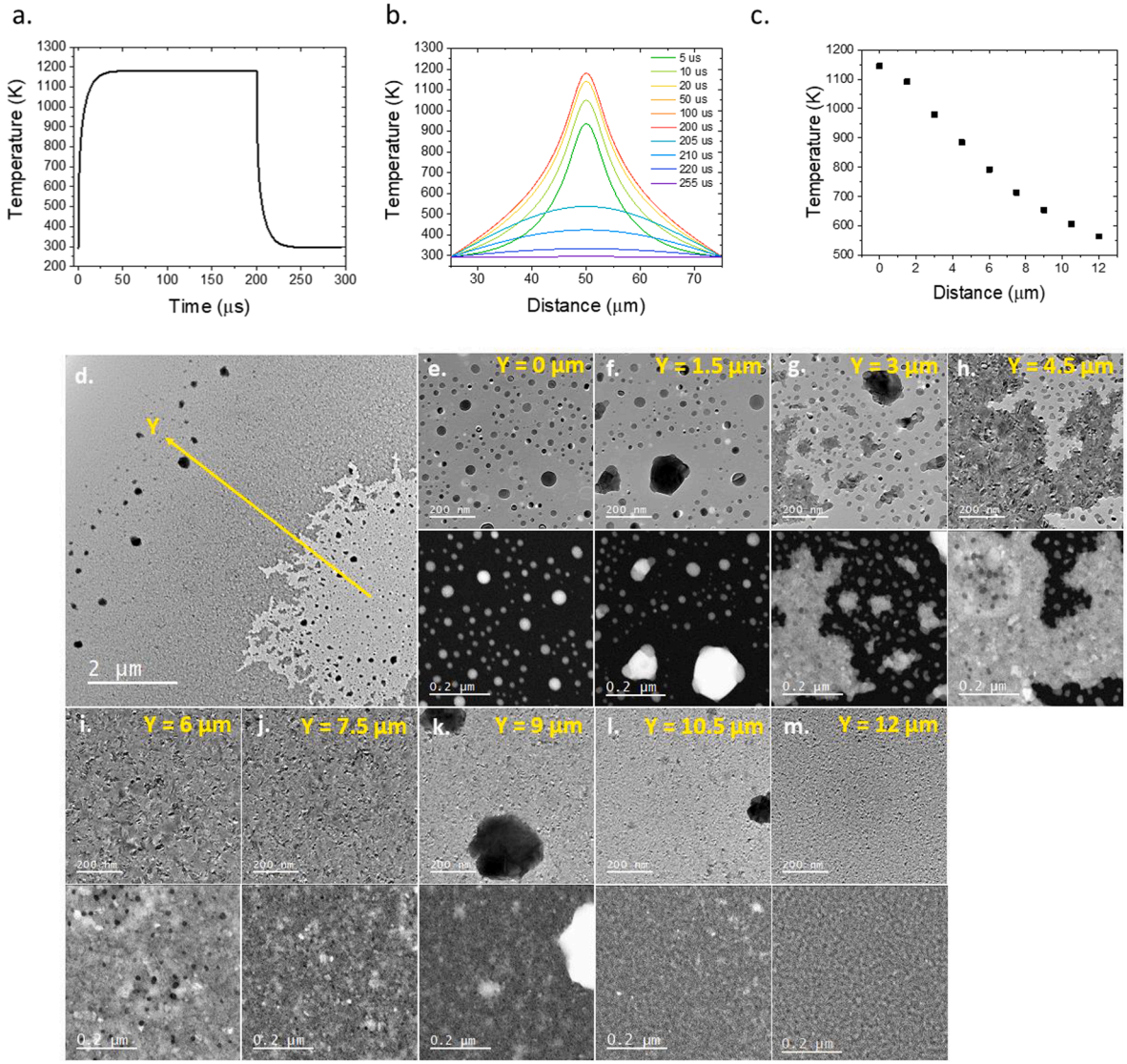

Fig. 6. (a) Time-temperature plot from a finite element photothermal simulation of a 20 nm thick $Ag_{0.5}Fe_{0.5}$ film on a 20 nm SiO_2 membrane exposed to a 25 mW laser. (b) Simulated surface temperature versus laser spot position for various times illustrating the spatial and temporal temperature evolution for a 25 mW power and 200 μs pulse width. (c) Plot correlating position of images taken in (e–m) to the relative annealing temperature, as shown in (b). (d) Micrograph overview of laser spot, with close up images taken 1.5 μm apart in (e–m). For each set of images, the bright field TEM image is above, and the HAADF STEM image is below.

To further explore the grain growth and phase separation in the Ag-Fe alloy, a 20 nm thick $Ag_{0.5}Fe_{0.5}$ film was sputtered onto a 20 nm SiO_2 TEM membrane then imaged after *in-situ* laser annealing. To induce grain growth and phase separation, the pulsed laser was focused at the TEM grid for five minutes at ≈25 mW, 200 μs at 100 Hz (2% duty cycle). The laser spot has an approximately Gaussian profile with a $1/e^2$ radius of ≈3.7 μm. Images were taken near the laser center every minute during the laser exposure (see Supplemental information S1). Subsequent to the laser exposure/heat treatment, TEM images, STEM images, and SAED patterns were taken every 1.5 μm up to 12 μm moving radially out from the spot center representing different annealing temperatures.

Fig. 6a–c illustrates a finite element thermal simulation based on the as-deposited index of refraction, as estimated via the spectroscopic ellipsometry and averaged physical properties of Ag and Fe (see Supplemental information S2 for table). As shown in Fig. 6a, the model predicts that the center of the beam reaches a steady-state maximum temperature of 1180 K in 55 μs and the peak temperature logically drops (Fig. 6b), to where the position 12 μm from the spot center reaches ≈560 K (Fig. 6c), well below the annealing temperature explored in the larger sample (873 K). Based on the ≈150 μs time at steady state per pulse, the cumulative annealing time at the maximal temperature is only 4.5 s (30,000 pulses).

A wide view image of the illuminated area is shown in Fig. 6d and highlights the position-dependent changes in the microstructure; the vector illustrating the sequence of images in Fig. 6e–m are shown as a yellow arrow. At the peak center (0 and 1.5 μm, Fig. 6e, f), solid state dewetting has occurred and nanoparticles result. The very center contains all spherical particles and the SAED pattern suggests that silver has preferentially evaporated due to its higher vapor pressure. This dewetting is shown in greater detail in Supplemental Fig. S3, where it is observed that, as the film dewets, a large (several micron) hole forms in the center of the laser spot. Because of this phenomenon, much of the energy in the center of the beam passes through the membrane rather than coupling to the deposited alloy, which in turn effects the annealing temperature of the film. To better understand these effects, several additional simulations were run with varied hole sizes, as shown in Supplemental Fig. S4.

At the 1.5 μm position (Fig. 6f), bi-metallic nanoparticles are evident where small Fe nanoparticles decorate larger silver cores and some small Fe-Ag Janus nanoparticles exist. At 3.0 μm and 4.5 μm (Fig. 6g, h) partial

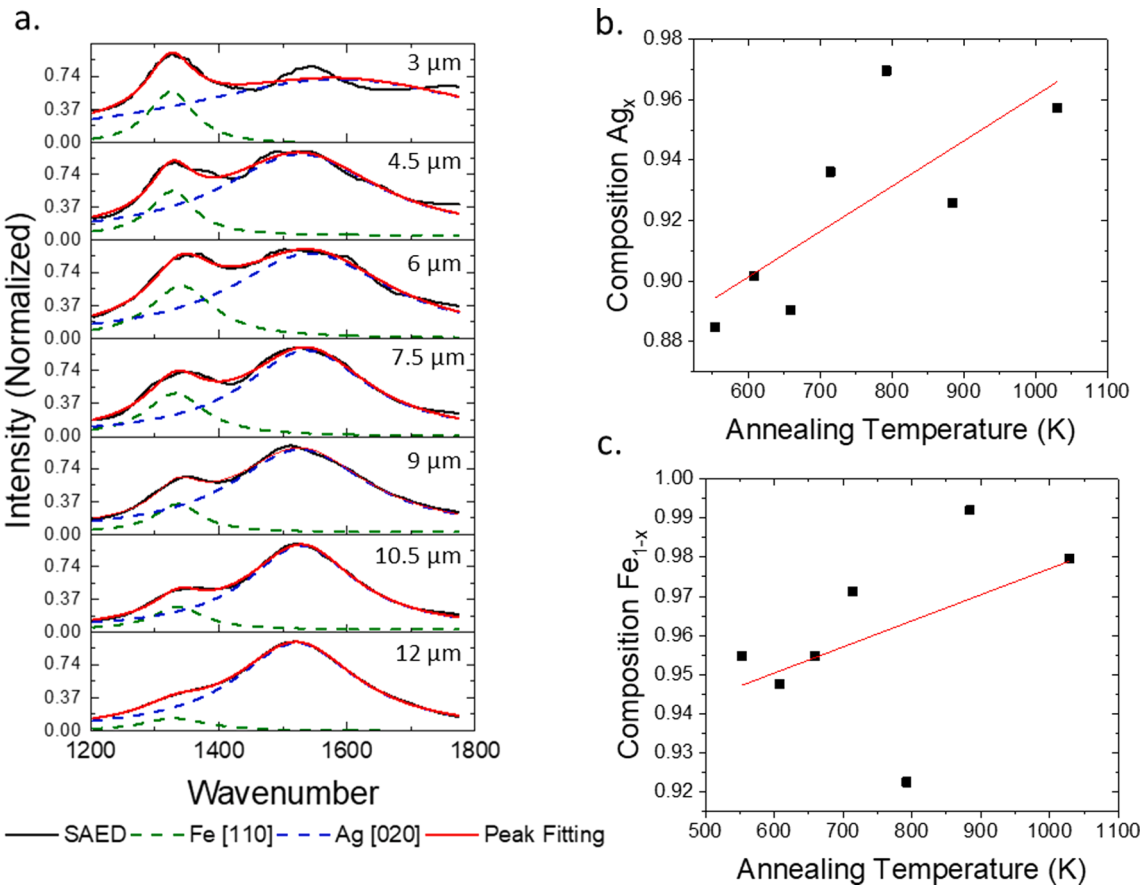

Fig. 7. (a) Radially averaged and normalized selected area electron diffraction patterns and fitted Ag and Fe peaks as a function of distance from the center of the laser spot, as shown in Fig. 6d. Composition of the Fe BCC (1 1 0) peak (b) and the Ag FCC (0 2 0) peak (c) plotted as a function of annealing temperature determined from Fig. 6 c.

dewetting is observed, and in the film regions, small scale phase separation and grain growth occurs. At radii >4.5 μm (Fig. 6i–m) dewetting does not occur and the degree of phase separation and grain growth decreases with increasing radius, eventually resembling the as-deposited condition at 12 μm. Interestingly, at ≈9 μm, corresponding to an annealing temperature of ≈650 K, large (several hundred nm) silver nanoparticles precipitate where the continuous films are nanogranular.

In agreement with the results shown in Fig. 5, the SAED shows that phase separation increases with increasing photothermal heating, as shown in Fig. 7. SAED measurements towards the center of the laser spot (Fig. 7a), indicate phase separation, as demonstrated by the shift to lower wavenumber of the Ag peak, and the shift to higher wavenumber of the Fe peak. Using the simulated laser conditions above, we can then correlate the shift in the Ag and Fe peaks to a necessary annealing temperature required to induce this shift, and shown in Fig. 7b, c. Note that the SAED measurements could not be performed at <3 μm from the center of the laser spot due to diffraction overexposure.

During the in-situ laser heating STEM experiments, phase separated nanoparticles were formed on the suspended membranes. Particles very similar to these have been described as “Nano-fried-eggs,” and are characterized by a FCC crystalized silver region surrounded by amorphous iron regions [21]. Low-loss EELS was used to measure the plasmonic spectrum of these nanoparticles. Fig. 8a shows the STEM image for one of these particles (a silver central region with two iron regions at the poles) and its associated EELS spectrum images b–d at various loss energies. For better visualization, the outline of the nanoparticle is superimposed over the spectrum images in black. In the Fe phase at the tips of the elongated nanoparticle, the bulk surface plasmon peaks can be clearly seen at 2.62 eV (b), as well as for another particle at the top of the image. A dipole peak associated with an ≈40 nm central Ag region is also observed at 3.05 eV (c), and is in good agreement with previous work on dewet silver nanoparticles of [22]. Finally, the silver bulk surface plasmon peak is observed at ≈3.50 eV (d).

As demonstrated in Fig. 8(a), various nanoparticle sizes and shapes were generated via the photothermal heating of the thin film. We envision that nanoparticle arrays of various sizes and compositions can be made via pulsed laser induced dewetting (PLID) [23]. The phase fraction of Ag and Ni can be controlled by the original thin film composition and the average particle size can be controlled by the thin film thickness. Furthermore, precise hierarchical one [24] and two [25] dimensional nanoparticle arrays can also be achieved. Thus, as we recently demonstrated in the Ag_xNi_{1-x} system [27] the dipolar plasmonic energy can be tuned by the resultant Ag nanoparticle volume and the magnetic moment per nanoparticle tuned by the Fe volume.

The saturation magnetization for five compositions between 15 at.% Fe and 78 at.% Fe, both annealed and as-deposited, were measured at 1.9 K and are tabulated in Fig. 9a. These results show a non-linear increase in the total moment approaching the Fe-rich samples, which does not change significantly with annealing. The non-linearity suggests that there may be some non-ferromagnetic ordering. Magnetization versus temperature measurements, shown in Fig. 8b, support this claim. Samples with 78 at.% Fe, 65 at.% Fe, and 50 at.% Fe show a distinct drop in the magnetization when cooling below 120 K, suggesting the onset of a new magnetic ordering. The M-T plots for the 30 at.% Fe and 15 at.% Fe do not have this drop. These plots all show a protracted shallow curve, suggesting that the Curie temperature, T_C, is well above 400 K, which is consistent for Fe – which has a T_C of 1043 K.

Magnetic hysteresis loops measured below 120 K show an enhanced

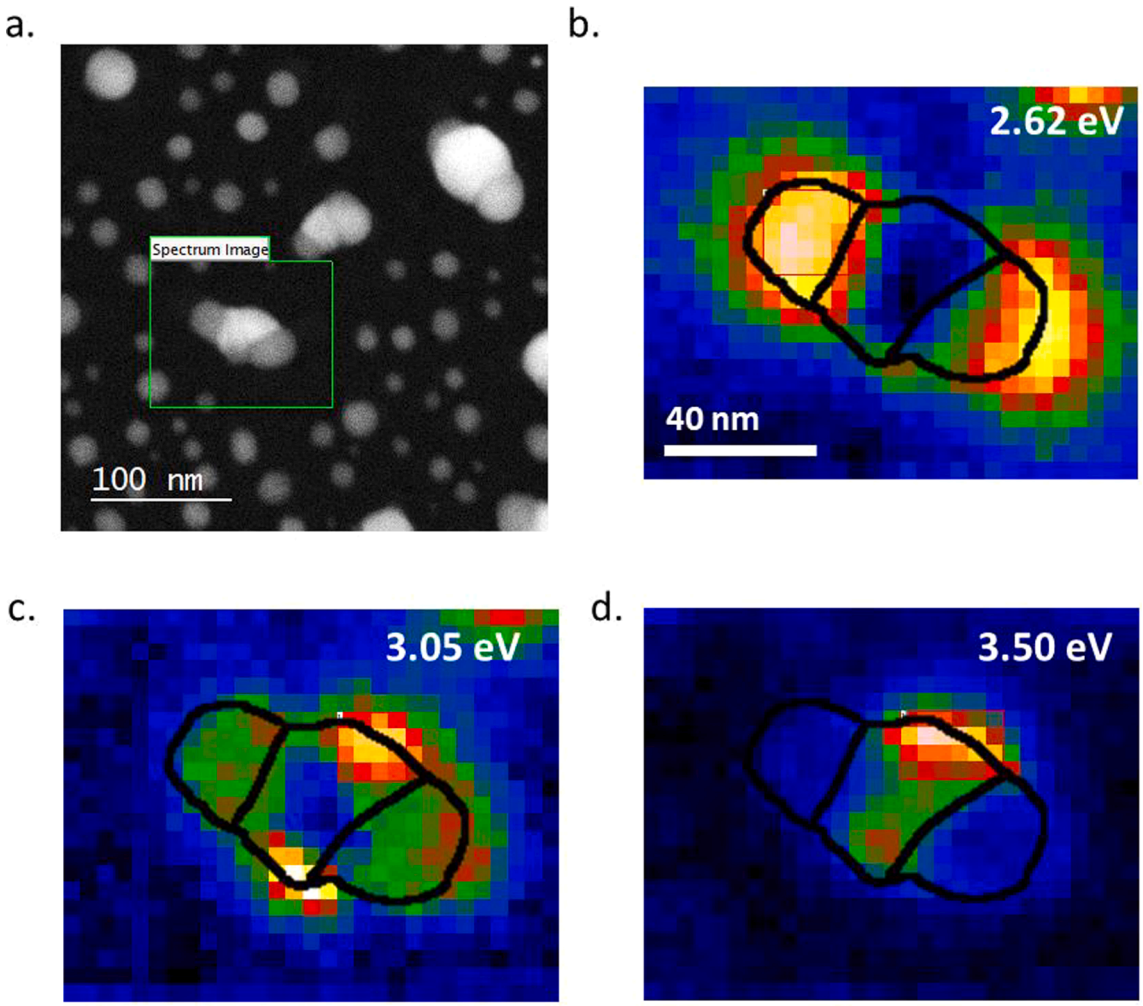

Fig. 8. (a) HAADF STEM image of an Ag-Fe nanoparticle, and associated EELS spectrum images for the (b) Fe bulk surface plasmon peak, (c) the Ag dipole peak, and (d) the Ag bulk surface plasmon peak. For a–c, the scale bar (shown in the bottom right corner of b) is 40 nm.

loop width (e.g. coercivity) and a shift along the field axis away from center (e.g. loop bias). These effects are well known and correspond to exchange bias, which results from the coupling between a ferromagnet and an antiferromagnet [28]. This suggests that the FeAg has an antiferromagnetic phase with a Néel temperature of ≈120 K, as suggested by the M-T plots. After annealing, the hysteresis loops measured above 120 K show an increased coercivity. This is likely due to pinning of the domain walls by Ag precipitates. Below 100 K the annealed loops also show an increase in the coercivity, albeit much smaller than the as-deposited sample, and also show no loop bias. This is likely a consequence of the phase separation, which reduces the antiferromagnetic phase fraction by precipitating separate Fe and Ag regions and decreases the contact boundary between the ferromagnetic and antiferromagnetic regions.

4. Conclusions

In conclusion, we have demonstrated that fast quenching in sputter deposited Ag_xFe_{1-x} results in a metastable supersaturated Ag-rich solid solution. Annealing of the films at 873 K for 1 h was sufficient for the solid solution to phase separate into the equilibrium Ag and Fe phases. The composition of the Ag_xFe_{1-x} alloy for both as deposited and annealed samples were analyzed via EDS, showing a silver gradient ranging from ($0.19 < x < 0.84$), allowing for the rapid characterization of the structural, optical and magnetic properties of the Ag_xFe_{1-x} system. The structural properties were characterized via SEM and TEM imaging, XRD, and SAED. The SEM and TEM imaging revealed no contrast in the as-deposited films, consistent with a nanogranular supersaturated solid solution. The annealed films revealed clear phase contrast indicative of the Ag and Fe phase separation. XRD and SAED patterns confirmed the observed phase separation in the annealed films. The optical properties were characterized via spectroscopic ellipsometry, and confirmed the expected decrease in the LSPR Q factor as the silver concentration increased. STEM of an annealed film resulted in phase separated Ag-Fe nanoparticles and the plasmonic properties were correlated via low-loss EELS. Finally, the magnetic behaviors of the films were analyzed by studying M-T and M-H measurements taken via a VSM and revealed a non-linear increase in the total moment approaching the Fe-rich samples, which suggests that there may be some non-ferromagnetic ordering. Magnetic hysteresis loops measured as a function of temperature revealed exchange bias below 120 K, which suggests that the Ag_xFe_{1-x} has an antiferromagnetic phase with a Néel temperature of ≈120 K. Thus, the demonstrated magnetic and plasmonic properties of phase-separated Ag_xFe_{1-x} alloys have promise in magnetoplasmonic applications such as combined magnetic resonance imaging and magnetically enhanced photothermal cancer therapy.

Declaration of Competing Interest

The authors declare that they have no known competing financial interests or personal relationships that could have appeared to influence the work reported in this paper.

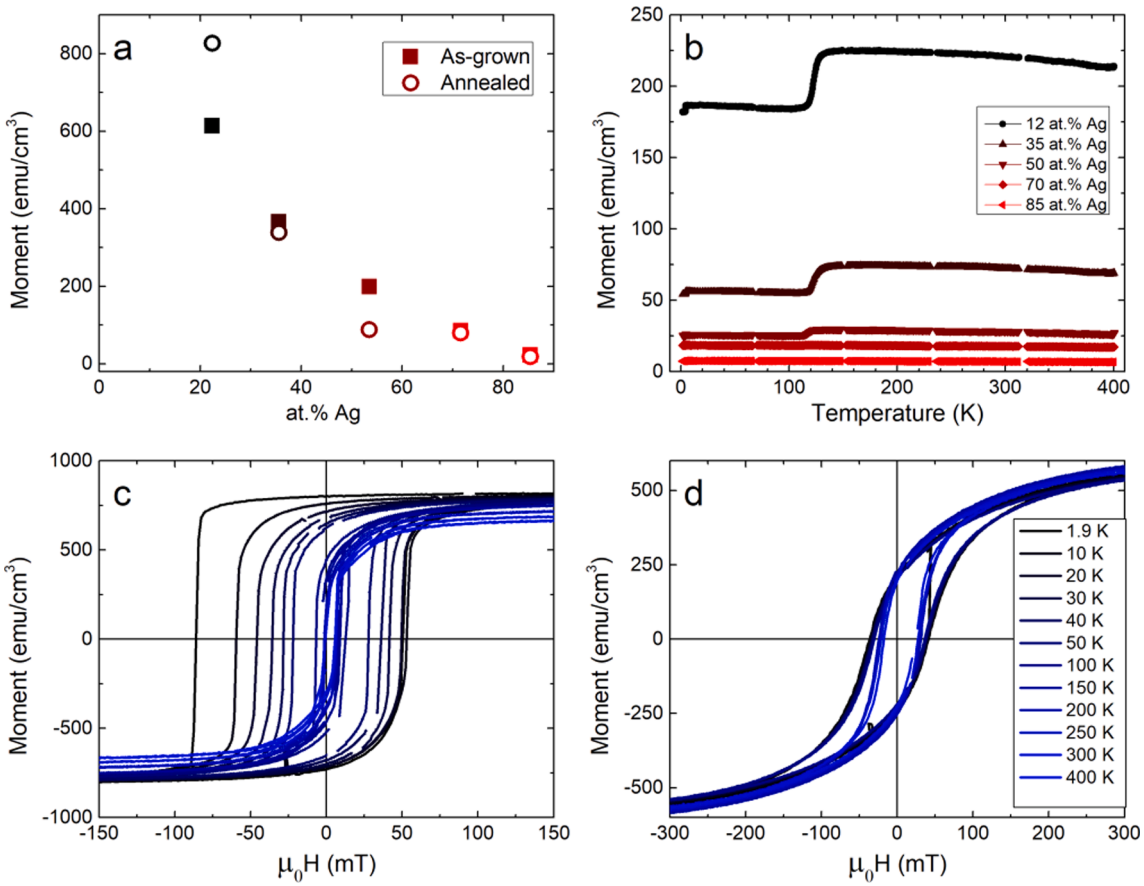

Fig. 9. (a) Saturation magnetization versus Ag composition, (b) M-T curves from the annealed samples, and major hysteresis loops for the 78 at.% Fe sample (c) as-deposited and (d) after annealing.

Acknowledgements

P.D.R. and R.C. acknowledge support from the National Science Foundation under grant NSF DMR 1709275. W.L.B. acknowledges support from the Center for Materials Processing and the Chancellor's Fellowship at the University of Tennessee. P.D.R. also acknowledges that the laser delivery system was built by Tom Moore and Greg Magel at Waviks Inc. and the system development is supported by NSF SBIR-1721719 and 1853201. D.A.Garfinkel acknowledges support from the National Science Foundation under grant NSF CBET 1603780. D.A. Gilbert and C.S.J acknowledge support by the U.S. Department of Energy, Office of Science, Office of Basic Research CAREER program under Award Number DE-SC0021344. The authors also acknowledge that the scanning electron microscopy was performed in the Nanofabrication Research Laboratory at the Center for Nanophase Materials Sciences, a DOE Office of Science user facility.

Data availability

The raw data required to reproduce these findings are available to download from [INSERT PERMANENT WEB LINK(s)]. The processed data required to reproduce these findings are available to download from [INSERT PERMANENT WEB LINK(s)].

Appendix A. Supplementary data

Supplementary data to this article can be found online at https://doi.org/10.1016/j.mseb.2021.115044.

References

[1] M.G. Blaber, M.D. Arnold, M.J. Ford, A review of the optical properties of alloys and intermetallics for plasmonics, J. Phys.: Condens. Matter 22 (14) (2010).
[2] V.J. Keast, R.L. Barnett, M.B. Cortie, First principles calculations of the optical and plasmonic response of Au alloys and intermetallic compounds, J. Phys.: Condens. Matter 26 (30) (2014).
[3] P.R. West, S. Ishii, G.V. Naik, N.K. Emani, V.M. Shalaev, A. Boltasseva, Searching for better plasmonic materials, Laser Photon. Rev. 4 (6) (2010) 795–808.
[4] C.M. Mueller, R.R. Murthy, M.R. Bourgeois, G.C. Schatz, Thermodynamic determination of bimetallic particle geometry: suitability of poorly miscible alloys for surface-enhanced Raman, J. Phys. Chem. C 124 (5) (2020) 3287–3296.
[5] J.G. Ovejero, et al., Synthesis of hybrid magneto-plasmonic nanoparticles with potential use in photoacoustic detection of circulating tumor cells, Microchim. Acta 185 (2) (2018).
[6] T.T. Nguyen, F. Mammeri, S. Ammar, Iron oxide and gold based magneto-plasmonic nanostructures for medical applications: a review, Nanomaterials 8 (3) (2018).
[7] I. Urries, et al., Magneto-plasmonic nanoparticles as theranostic platforms for magnetic resonance imaging, drug delivery and NIR hyperthermia applications, Nanoscale 6 (15) (2014) 9230–9240.
[8] K. Sumiyama, Y. Yoshitake, Y. Nakamura, Thermal stability of high concentration Fe-Cu alloys produced by vapor quenching, Acta Metall. 33 (1985) 1785–1791.
[9] K. Sumiyama, K. Takemura, N. Kataoka, Y. Nakamura, Effect of Ar gas pressure on morphology and structure of nonequilibrium Fe-Cu alloys produced a by rf sputtering, Trans. Japan Inst. Met. 29 (12) (1988) 962–969.
[10] A. Tomitaka, et al., Development of magneto-plasmonic nanoparticles for multimodal image-guided therapy to the brain, Nanoscale 9 (2) (2017) 764–773.
[11] C.H. Wu, J. Cook, S. Emelianov, K. Sokolov, Multimodal magneto-plasmonic nanoclusters for biomedical applications, Adv. Funct. Mater. 24 (43) (2014) 6862–6871.
[12] I.S. Maksymov, Magneto-plasmonic nanoantennas: basics and applications, Rev. Phys. 1 (2016) 36–51.
[13] Y. Nakamura, K. Sumiyama, Y. Nakamura, Magnetic properties of high-concentration Fe-Ag alloys produced by vapor quenching, J. Phys. F: Met. Phys. 15 (1985) 1405–1411.
[14] M. Takao, H. Senno, Insoluble binary system thin film, J. Magn. Magn. Mater. 31–34 (Part 2) (1983) 949–950.

[15] K. Sumiyama, Y. Nakamura, Magnetic properties of metastable crystalline and amorphous Fe alloys produced by RF sputtering, J. Magn. Magn. Mater. 35 (1983) 219–220.
[16] U. Herr, J. Jing, U. Gonser, H. Gleiter, Alloy effects in consolidated binary mixtures of nanometer-sized crystals investigated by Mössbauer spectroscopy, Solid State Commun. 76 (2) (1990) 179–202.
[17] J.H. Li, Y. Kong, K.W. Geng, B.X. Liu, Positive correlation between the magnetic moment of Fe and atomic volume in the binary Fe-(Cu, Ag, Au) alloys revealed by ab initio calculations, Scr. Mater. 57 (2) (2007) 105–108.
[18] Y. Wu, et al., Exploring photothermal pathways via in situ laser heating in the transmission electron microscope: recrystallization, grain growth, phase separation, and dewetting in $Ag_{0.5}Ni_{0.5}$ thin films, Microsc. Microanal. 24 (6) (2018) 647–656.
[19] R. Collette, Y. Wu, P.D. Rack, Correlating the optical property evolution in the Au-Ni binary thin films: from metastable solid solution to phase separated alloy, J. Alloys Compd. 793 (2019) 695–704.
[20] J.D. Fowlkes, J.M. Fitz-Gerald, P.D. Rack, Ultraviolet emitting $(Y_{1-x}Gd_x)_2O_{3-\delta}$ thin films deposited by radio frequency magnetron sputtering: combinatorial modeling, synthesis, and rapid characterization, Thin Solid Films 510 (1–2) (2006) 68–76.
[21] J. Ramade, et al., Nano-fried-eggs: Structural, optical, and magnetic characterization of physically prepared iron-silver nanoparticles, Nano Res. 11 (11) (2018) 6074–6085.
[22] G. Li, et al., Examining substrate-induced plasmon mode splitting and localization in truncated silver nanospheres with electron energy loss spectroscopy, J. Phys. Chem. Lett. 6 (13) (2015) 2569–2576.
[23] L. Kondic, A.G. González, J.A. Diez, J.D. Fowlkes, P. Rack, Liquid-state dewetting of nanoscale metal films and other geometries, Annu. Rev. Fluid Mech. 52 (2020) 235–262.
[24] J.D. Fowlkes, et al., Hierarchical nanoparticle ensembles synthesized by liquid phase directed self-assembly, Nano Lett. 14 (2014) 774–782.
[25] Y. Wu, et al., Directed liquid phase assembly of highly ordered metallic nanoparticle arrays, ACS Appl. Mater. Interfaces 6 (2014) 5835–5843.
[27] David A. Garfinkel, Grace Pakeltis, Nan Tang, Ilia N. Ivanov, Jason D. Fowlkes, Dustin A. Gilbert, Philip D. Rack, Optical and Magnetic Properties of Ag−Ni Bimetallic Nanoparticles Assembled via Pulsed Laser-Induced Dewetting, ACS Omega 5 (30) (2020) 19285–19292, https://doi.org/10.1021/acsomega.0c02894.
[28] J. Nogués, I.K. Schuller, Exchange bias, J. Magn. Magn. Mater. 192 (2) (1999) 203–232.